Northumbria Research Link

Citation: Naylor, Matthew, Tiwari, Devendra, Sheppard, Alice, Laverock, Jude, Campbell, Stephen, Ford, Bethan, Xu, Xinya, Jones, Michael, Qu, Yongtao, Maiello, Pietro, Barrioz, Vincent, Beattie, Neil, Fox, Neil A., Fermin, David J. and Zoppi, Guillaume (2022) Ex-situ Ge-doping of CZTS Nanocrystals and CZTSSe Solar Absorber Films. Faraday Discussions. ISSN 1364-5498 (In Press)

Published by: Royal Society of Chemistry

URL:

This version was downloaded from Northumbria Research Link: http://nrl.northumbria.ac.uk/id/eprint/49001/

Northumbria University has developed Northumbria Research Link (NRL) to enable users to access the University's research output. Copyright © and moral rights for items on NRL are retained by the individual author(s) and/or other copyright owners. Single copies of full items can be reproduced, displayed or performed, and given to third parties in any format or medium for personal research or study, educational, or not-for-profit purposes without prior permission or charge, provided the authors, title and full bibliographic details are given, as well as a hyperlink and/or URL to the original metadata page. The content must not be changed in any way. Full items must not be sold commercially in any format or medium without formal permission of the copyright holder. The full policy is available online: http://nrl.northumbria.ac.uk/policies.html

This document may differ from the final, published version of the research and has been made available online in accordance with publisher policies. To read and/or cite from the published version of the research, please visit the publisher's website (a subscription may be required.)

Northumbria University NEWCASTLE

CUSTOMER SERVICE EXCELLENCE CSE

UniversityLibrary

Ex-situ Ge-doping of CZTS Nanocrystals and CZTSSe Solar Absorber Films

Matthew C. Naylor[1], Devendra Tiwari[1,2], Alice Sheppard[2], Jude Laverock[3], Stephen Campbell[1], Bethan Ford[1], Xinya Xu[1], Michael Jones[1], Yongtao Qu[1], Pietro Maiello[1], Vincent Barrioz[1], Neil S. Beattie[1], Neil A. Fox[2,3], David J. Fermin[2], Guillaume Zoppi[1]

[1] *Department of Mathematics, Physics and Electrical Engineering, Ellison Building, Northumbria University, Newcastle Upon Tyne, NE1 8ST, United Kingdom*
[2] *School of Chemistry, University of Bristol, Cantock's close, Bristol BS8 1TS, United Kingdom*
[3] *H.H. Wills Physics Laboratory, University of Bristol, Tyndall Av., Bristol BS8 1TL, United Kingdom*

Abstract

$Cu_2ZnSn(S,Se)_4$ (CZTSSe) is a promising material for thin-film photovoltaics however the open-circuit voltage (V_{OC}) deficit of CZTSSe prevents device performance to exceed 13% conversion efficiency. CZTSSe is a heavily compensated material that is rich in point defects and prone to the formation of secondary phases. The landscape of these defects is complex and some mitigation is possible by employing non-stoichiometric conditions. Another route used to reduce the effects of undesirable defects is doping and alloying of the material to suppress certain defects and improve crystallization such as germanium. The majority of works deposit Ge adjacent to a stacked metallic precursor deposited by physical vapour deposition before annealing in a selenium rich atmosphere. Here we use an established hot-injection process to synthesise Cu_2ZnSnS_4 nanocrystals of a pre-determined composition, subsequently doped with Ge during selenisation to aid recrystallisation and reduce the effects of Sn species. Through Ge incorporation we demonstrate structural changes with negligible change in energy bandgap but substantial increase in crystallinity and grain morphology which is associated to a Ge-Se growth mechanism and gains in both V_{OC} and conversion efficiency. We use surface energy-filtered photoelectron emission microscopy (EF-PEEM) to map the surface work function terrains and show an improved electronic landscape which we attribute to a reduction in segregation of low local effective work function (LEWF) Sn(II) chalcogenide phases.

Introduction

$Cu_2ZnSn(S,Se)_4$ (CZTSSe) is a promising material for thin-film photovoltaics whose core constituent elements are Earth abundant and non-toxic. CZTSSe is an attractive material due to its close relation to the commercially-established $Cu(In,Ga)Se_2$ photovoltaic technology and thus, the potential for knowledge transfer between analogues. The open-circuit (V_{OC}) deficit of CZTSSe devices is severe and prevents device performance to exceed conversion efficiencies of ~12.7%[1, 2]. A large portion of this deficit is associated with atomic disorder in the lattice giving rise to a complicated landscape of point defects and problematic coupling of defects or so-called defect complexes[3]. The current understanding in literature surmises that a Cu-poor and Zn-rich stoichiometry can supress the formation of some point defects and secondary phases but alas, the potent V_{OC} deficit is still observed[4]. Sn-related defects, namely the Sn_{Zn} antisite defect have been identified to be particularly detrimental through the facilitation of mid-band charge carrier recombination sites which pin the V_{OC} to sub-energy bandgap (E_g) potentials[5, 6]. The multivalency of Sn permits different valence of the Sn_{Zn} antisite defect, and as such Sn^{2+}_{Zn} and Sn^{4+}_{Zn} coexist. The coupling of Sn^{2+}_{Zn} with the abundant Cu^{+}_{Zn} antisite defect forms the cluster $[Sn^{2+}_{Zn} + 2Cu^{+}_{Zn}]$, which has been reported to cause band-tailing and further restricts the V_{OC}[7]. One method to change the electric properties CZTSSe is to alloy or extrinsically dope the material; elements such as Ag[8], Cd[9], Ge[10, 11] and Sb[12, 13] have been used to moderate success. It is important to distinguish between doping and alloying when studying these mechanisms as the former, involves nominal quantities in an effort to affect the electronic properties whereas the latter, involves significantly greater quantities which fundamentally change the electronic and structural identity of the compound – this distinction has been comprehensively reviewed in literature[14].

Considering the potential origins of the V_{OC} deficit, Sn sites are a clear target for doping and alloying, Ge emerges as an obvious candidate due to elemental grouping. Ge incorporation, despite its elemental cost and abundance, remains a fruitful platform to investigate electronic effects which could later be reproduced by alternative means once further understood. Ge has consistently proven to result in enhanced device performance, namely V_{OC}, with the majority of studies probing the effects of Ge to bulk recombination pathways[10, 11, 15-19]. Although, to fully understand the role of Ge plays in improving the device performance and in particular, V_{OC} losses, here for the first time, we analyse the surfaces of CZTSSe films with Ge doping with energy-filtered photoelectron emission microscopy (EF-PEEM) to map the surface work function terrains. This would provide insights into the possible recombination prevalent at CZTSSe/CdS interface and physico-chemical mechanism of Ge's role in reducing these shunting pathways.

To date, the majority of Ge doping studies have used a sacrificial Ge layer to dope a metallic precursor stack deposited by vacuum-based techniques[10, 16, 18] or have used a chemical route to introduce significant quantities of Ge *during or prior to* the formation of a Cu_2ZnSnS_4 (CZTS) compounds, also referred as in-situ doping or alloying[11, 20]. In this study we introduce Ge independently to the formation of CZTS, via the so-called ex-situ route, to decouple the effects of Ge with premature phases (binary and ternary chalcogenides) and investigate the effect of Ge doping has on the transition from CZTS to CZTSSe. To achieve this ex-situ doping effect we unusually combine solution and physical vapour deposition techniques such that, solution processed quaternary CZTS precursors are combined with elemental Ge films using a separate vacuum-based deposition step. This approach somewhat isolates the doping mechanisms which allows this work to probe enhanced grain growth, Ge-Sn interactions and the suppression of Sn disorder at a Sn-rich CZTSSe/CdS interface in new light.

Results and discussions

CZTS crystalline nanoparticles, known herein has as nanocrystals (NCs) were synthesised using a hot-injection method and re-dispersed to form a NC-based ink[21]. Slot-die coating was used to deposit the NC based-ink and form the quaternary precursor layer, a thickness of 800 nm is achieved by successive coatings with an intermediate soft-baking step of films at 300°C in air. The precursor films were then selenised and annealed under an Se-Ar_2 atmosphere at 500°C for 20 minutes. Ge was incorporated by electron beam evaporation of elemental Ge underlayer 5, 15, 50 nm prior to CZTS precursor deposition. Accordingly, the samples are labelled as 'CZTSSe', 'Ge5:CZTSSe', 'Ge15:CZTSSe' and 'Ge50:CZTSSe', for CZTSSe films with no Ge, and with 5 nm, 15 nm and 50 nm of Ge underlayer, respectively. Other strategies of incorporating the Ge into CZTSSe layer were also explored, including the addition of Ge layers after the precursor deposition step, which upon selenisation led to a graded Ge profile with dominant distribution limited to the CZTSSe front surface. Thus, suggesting poor incorporation of Ge and perhaps volatilisation of Ge-chalcogenide phases (Ge_xSe_y) during annealing, which are known to have low melting points relative to other metallic phases[22] – notably similar when Se-rich stoichiometry to the renowned Sn_xSe_y species[23]. However, addition of Ge as an underlayer to CZTSSe films results in retention of nominal Ge concentration in the films. **Figure 1a** shows the elemental depth profile of Ge across the thickness of precursor CZTS films overlaid on cross-section micrograph, which demonstrates that Ge distribution remains concentrated at Mo/CZTS interface after successive soft baking steps. **Figure 1b** shows the secondary ion mass spectroscopy (SIMS) depth profiles of Ge across CZTSSe devices along with Cu and Mo as indicators of the Mo/CZTSSe structure for undoped and 50 nm Ge underlayer. It is clear that upon selenisation Ge diffuses homogenously over the entire CZTSSe film. Considering the absorber thickness of 1 μm, a 5 nm Ge underlayer will correspond to a nominal doping equivalent to 0.06 atomic % and similarly 15 nm and 50 nm Ge will be equivalent to 0.18% atomic % and 0.6 atomic %, respectively. The solar cell devices were completed in a substrate architecture with a SLG/Mo/(Ge)/CZTSSe/CdS/i-ZnO/ITO/Ni-Al structure. Further details of sample preparation are available in the experimental section.

Figure 2 depicts the structural properties of selenised CZTSSe and Ge:CZTSSe films probed by X-ray diffraction (XRD). XRD patterns (**Figure 2a**) are consistent with the formation of pure kesterite phase (I-4). No additional peaks due to secondary phases are visible confirming the phase-purity of the films.

Comparison of observed XRD patterns with the Bragg reflections of ICDD standards for Kesterite Cu_2ZnSnS_4 and $Cu_2ZnSnSe_4$, suggests a nearly complete selenisation of the CZTS precursor films. The addition of Ge to CZTSSe systematically shifts the peak position of Sn dominated planes to larger angles (see **Figure 2b** for (002) example while the planes without Sn show only marginal changes. This is indicative of Ge substitution at isoelectronic Sn-site within lattice. Furthermore, the peaks undergo a relative increase in intensity of 66%, 168% and 224% for Ge5:CZTSSe, Ge15:CZTSSe and Ge50:CZTSSe films, respectively, compared to CZTSSe films, as well as narrowing of peak widths, which means improved crystallisation with Ge incorporation. Consequently, average crystallite sizes in CZTSSe, Ge5:CZTSSe, Ge15:CZTSSe and Ge50:CZTSSe films calculated using Scherrer equation from the (002) peaks (**Figure 2c**), increase from 40 to 88 nm. The scanning electron microscopy (SEM) cross-sectional images of CZTSSe and Ge50:CZTSSe solar devices (**Figure 3)**, evidence a significant increase in grain sizes from < 1 μm to > 1 μm laterally and a grain structure spanning across the thickness of absorber upon doping . Consequently, this enlarged grain sizes can qualitatively be correlated to an increased surface roughness through inspection of the transparent conducting oxide (TCO) layer morphology, shown in the upper section of the micrographs (**Figure 3**).

The phase purity of CZTSSe films is also corroborated with Raman spectroscopy (**Figure 4a)**, with all films displaying A-symmetry modes at around 174 cm^{-1}, 179 cm^{-1} and 199 cm^{-1} associated with the kesterite phase. Comparing the observed Raman shifts to those reported for CZTS-Se solid mixtures, suggests nearly complete selenisation of the precursor CZTS films. No other peaks due to secondary phases were detected using the 633 nm excitation wavelength. Ge doping, especially Ge50:CZTSSe, shows an blue-shift of about 1 cm^{-1} relative to CZTSSe films, as has been previously reported and confirms inclusion of Ge in CZTSSe lattice[18] (**Figure 4b**). Additionally, Ge addition to CZTSSe films results in an increased asymmetry of the peaks (**Figure 4b**), which has been associated previously with degree of disorder in Ge:CZTSSe prepared by sputtered absorbers.

The elemental atomic ratios of Sn(Ge)/(Cu+Zn+Sn), Cu/(Zn+Sn) and Se/(S+Se) derived from quantitative energy dispersive X-ray spectroscopy (EDS) are presented in **Figure 5**. Cu/(Zn+Sn) and Se/(S+Se) remain confined closely to 0.813 ± 0.008 and 0.963 ± 0.018, respectively, thus confirming of a nearly selenised stoichiometry. Interestingly, the Sn concentration decreases systematically with Ge addition to the films; thus, suggesting Ge substitution on Sn atoms in the lattice during annealing. In contrast to the bulk, the surface composition of CZTSSe films measured by X-ray photoelectron spectroscopy (XPS) analysis determined Zn/Sn and Cu/(Zn+Sn) ratios of 0.360 and 0.848 for CZTSSe and 0.466 and 0.763 for Ge5:CZTSSe, respectively, indicating a significant Zn-poor surface composition. Additionally, Se/(S+Se) ratios of 0.735 and 0.715 for CZTSSe and Ge5:CZTSSe, respectively, suggesting a more sulphur rich sulphur composition than bulk of 22% compared to 4%. These contrasting stoichiometries at the film surface to that of the bulk would crucially govern the interfacial properties and thus the work function landscape and device performance.

Figure 6a depicts the current density-voltage (JV) characteristics of representative SLG/Mo/(Ge)CZTSSe/CdS/i-ZnO/ITO/Ni-Al solar cells, measured under simulated AM1.5G spectrum with power density of 100 mW/cm^2. The total area of the devices was 0.16 cm^2. There is statistically significant improvement in all the key performance metrics of open-circuit voltage (V_{OC}), short-circuit current density (J_{SC}) and efficiency upon Ge doping (**Figure 6b**). Doping with 5 nm of Ge leads to a consistent increase of >1% in efficiency. Particularly, V_{OC} increases with Ge content by up to 25 mV. J_{SC} on the other hand, achieves a maximum for Ge15:CZTSSe cells primarily due to increased charge carrier diffusion enabled by larger grain sizes. A reduced J_{SC} for Ge50:CZTSSe could be due to higher recombination rate. However, the doping with thicker underlayer of 50 nm doesn't cause significant further improvement as the increase in the V_{OC} is compensated by a saturation of J_{SC} as well as the inhomogeneous trend in fill factor. Interestingly, the trend in fill factor mirrors the trend of asymmetry in Raman A mode at 199 cm^{-1} (**Figure 4b**), which could imply a correlation of recombination with the degree of disorder as indicated by the asymmetry of Raman spectral peak.

The spectral response analysis of external quantum efficiency (EQE) for the devices is presented in **Figure 7**. **Figure 7a**, shows a similar EQE spectra for all the devices at wavelengths below the absorption edge while disregarding the inconsistencies in device fabrication due to thickness and quality of the buffer and TCO layers produced over a disrupted period of time (400 nm < λ < 700 nm). Notable

differences are apparent in the absorption edge reflecting the changes to the CZTSSe layer due to Ge doping (1000 nm < λ < 1400 nm). The first derivative of EQE with wavelength, depicted with vertical dotted line, highlights a dual edge behaviour (**Figure 7b**). The first inflexion point occurs at a transition energy of ~1.18 eV and remains constant across all samples, while the inflexion peak at ~1.13 eV shows a reduction with Ge amount thus, suggesting this could be associated to a secondary phase in the CZTSSe phase which ameliorates with Ge doping. The observed transition energy of 1.13 eV is close to the band gap of isostructural tetragonal Cu_2SnS_3[24], which is a possibility given the very Zn poor surface composition. With Ge doping this inflexion reduces which again correlates with increase in Zn concentration at the surface, this also matches with a lowering in the Urbach energy (E_U) of tail states often associated with Cu-Zn disorder in CZTSSe devices (**Figure 7c**). The consistency of 1.18 eV inflexion peak suggests this is due to the bandgap of the CZTSSe, which is unexpectedly high for a 96% selenised CZTSSe. Comparing with previous measurement of bandgaps versus chalcogen ratio, with bandgaps of $Cu_2ZnSnSe_4$ and Cu_2ZnSnS_4 of 1 and 1.5 eV and bowing parameter of 0.18[25], 1.18 eV corresponds to 69% Se/(S+Se) which is in close agreement with the surface Se/(S+Se) ratios estimated from XPS measurements.

Local effective work function (LEWF) maps of CZTSSe films were constructed from EF-PEEM spectroscopy measurements. **Figure 8** contrasts the LEWF for CZTSSe and Ge5:CZTSSe films. The LEWF map of CZTSSe without Ge displays a significant presence of low LEWF regions, as can be further visualised from the tailing of the LEWF distribution profile. The appearance of such low LEWF regions has previously correlated to the existence of surface confined Sn (II) chalcogenide phases[26]. This hypothesis further corroborates with Sn-rich composition of CZTSSe films as determined from XPS. The addition of Ge leads to a significant dampening of the low work function regions and a smoother surface energy landscape, as is further apparent from the absence of tailing of the LEWF distribution profile. The average LEWF of the sample without and with Ge doping, however, remains the same at around 4.54 eV. Work function of n-CdS has been reported between 3.8-4.0 eV from UV-photoelectron spectroscopic analysis of a CZTSSe/CdS device[27]. Considering similar band-alignment, a built-in field of ~0.65 eV is expected which is significantly lower than the bandgap of CZTSSe films and thus explains the observed low V_{OC} of devices. We believe, this is due to the presence of Cu-Sn chalcogenide phases as suspected from the dual-edge behaviour seen in the EQE spectra. However, Ge incorporation improves the V_{OC} and FF of devices, primarily by reducing the segregation of low-LEWF Sn(II) chalcogenide phases at the CZTSSe/CdS interface, thus decreasing shunting of carriers across of interface. Furthermore, the LEWF distribution (**Figure 9c,d)** shows a large broadening of LEWF profile upon Ge incorporation (89.7 meV versus 138.2 meV without and with a 5 nm Ge underlayer, respectively). As in our previous EF-PEEM studies on CZTS and CZTSSe films derived from a molecular solution, we believe this can be associated to an increased Cu-Zn disorder in the films[12, 28]. This is also in agreement with the increased asymmetry of Raman modes observed in the films.

To gain a mechanistic insight into the role of Ge doping in CZTSSe films we deliberately induced accelerated segregation of Sn at the surface by heating the CZTSSe films under ultra-high vacuum (UHV) conditions at 300°C for 1 hour. From the previous studies, supported by SIMS analysis, Siebentritt et.al. have demonstrated the preferential migration of Sn towards front surfaces upon annealing[1, 29, 30]. **Figure 9a** presents the LEWF map and distribution from CZTSSe films upon UHV heat-treatment, which clearly show a large all-around decrease in LEWF, converging to values close to the low-LEWF regions as seen in **Figure 8a** for the CZTSSe without Ge and heat treatment. This confirms extensive Sn-migration to the CZTSSe film surface. Notably, **Figure 9b** shows CZTSSe with a 50 nm Ge underlayer upon similar heat treatment greatly retains the LEWF distribution close to CZTSSe films not subjected to UHV heat treatment. This is a remarkable finding, indicating the strong thermodynamic stabilisation of CZTSSe structure upon Ge doping. This increased stability is in good agreement with the work from Kim et al., who inferred a larger alloy stability for Ge-doped CZTSe through a reduced interaction parameter[10]. This finding also suggests that Ge introduced through an ex-situ doping route has a limited effect on somewhat crystalline phases but can however interact with segregated phases.

In addition to the interface, ex-situ Ge-doping clearly has implications to the bulk in terms of grain morphology as seen in **Figure 3**, a mechanism we postulate is activated by Se vapour during

selenisation. This Ge-Se interaction is reported to aid the crystallisation process through the formation Ge_xSe_y liquid phases, such as Ge_3Se_7, which could form a flux during selenisation[16, 17]. Introduction of $GeSe_2$ has also been reported to act in a similar fashion once stabilised in a liquid $GeSe_2$-Se system[10, 19]. For both analogues, and in this study, the formation of a flux means greater atomic mass transport thus, resulting in increased grain growth assisted by these growth mechanisms. Larger grains naturally lead to a reduction in grain boundaries for a film of similar thickness and are also associated with polycrystalline films of greater quality thus, reducing the number of structural defects. The effect on electronic defects cannot be quantitively described from this study however, it is reasonable to assume that the increased in V_{OC} is not solely derived from the interface and that improvement in bulk defects jointly contributes. **Figure 5** portrays a composition ratio shift in (IV)/(I + II + IV) that is compensated with respect to increased Ge doping. This Ge compensation could supress Cu_{Sn} antisite defects which have been widely reported caused Sn loss during selenisation[31, 32]; this suppression of trap states is a long-proposed mechanism in Ge doping and alloying[10, 15, 17]. The suppression management around the Sn site may reduce the magnitude of decomposition of CZTSSe and by proxy the amount of multivalency related to Sn[32], as well as the defects and related band-tailing associated with Sn^{2+}_{Zn} [7] – this is one possible narrative for the decrease in E_U depicted in **Figure 7c**. The retention of performance in devices with thick Ge underlayers suggests that ex-situ doping has a wider operating window with respect to nanometric incorporation, this also indicates the difficulty to dope crystallised quaternary precursors efficiently. This difficulty has also been reported in preliminary work by Neuschitzer et al. in which Ge was introduced to a highly crystallised film in a so-called post deposition treatment, although this route did not yield satisfactory results and so Ge introduction to a nanocrystalline film was necessary[15]. Compared to other works we do not observe a severe deterioration in performance metrics for devices doped with large quantities of Ge – a characteristic likely due to the nature of ex-situ doping. The persistent V_{OC} metric indicates that the level of Ge doping has not yet saturated the bulk, this saturation has been reported to cause the formation of Ge_{Cu} antisite defects in Cu-poor devices and form a deep level charge carrier recombination centre[15].

Conclusion

In this work we describe an ex-situ Ge doping route for CZTSSe films and solar cell devices using quaternary precursors. We describe nominal Ge incorporation through elemental depth profiling, systematic structural change whilst a negligible change in energy bandgap is measured. This set of characteristic changes evidences Ge doping appose to alloying. Using diffractograms and cross-sectional micrographs we observe a substantial increase in crystallinity and grain morphology which is associated to a Ge-Se growth mechanism. Surface EF-PEEM measurements show an improved electronic landscape which we attribute to a reduction in segregation of low-LEWF Sn(II) chalcogenide phases. To further improve this landscape co-doping with alkali metals, in particular Na, should be investigated to smooth the landscape further. The stability of the alloy under UHV heating showing promise for the stability of the alloy, this is a key characteristic of the material within the wider photovoltaic materials subject area at present. Through the statistical analysis of JV metrics, we report a beneficial impact for ex-situ Ge doping including an increased V_{OC}. We also report no large decline in performance with higher Ge doping amounts, which suggests a limited impact that this ex-situ doping route can facilitate. To further explore ex-situ doping, Ge could be introduced chemically after the NC synthesis to obtain a wider distribution not reliant on high temperature annealing. Finally, we compare bulk and interface mechanisms for V_{OC} loss laying the path for further surface measurements and mandating a systematic investigation of bulk recombination mechanisms in Ge:CZTSSe thin film solar cells.

Experimental Methods

a. Sample preparation

Molybdenum deposition: prior to the deposition of Mo back contact layer, soda-lime glass (SLG) substrates were cleaned in an ultrasonic bath of Decon90®, rinsed with deionised (DI) water and dried with a jet of N_2. The cleaned SLG substrates were DC-sputtered with Mo of 850 nm.

CZTS nanocrystal synthesis: CZTS nanocrystals were synthesised by our hot-injection recipe reported previously in greater details. For this, metal salts and sulphur are dissolved in oleylamine before being combined in a controlled reaction. The NCs are then collected and washed with solvents using centrifugation before finally being dispersed in toluene – this process has been described in greater detail elsewhere[33]. The synthesised NCs were then redispersed in 3 ml of 1-hexanthoil to form a concentrated CZTS NC-based ink (~200 mg/mL)[21].

CZTS precursor film deposition: CZTS NC-based ink was deposited on Mo-coated SLG substrates using slot-die coater from Ossila, equipped with a single 100 μm shim located between two coating head pieces. To yield a uniform layer ~260 μL of ink was used to form the initial menisci, coating speed was 40 mm s^{-1}, dispense rate was 18.2 μL s^{-1}, gap height was 800 μm, stage temperature was set to 80 °C. An 800 nm thick precursor was built up by 4 single pass coatings, after each layer the sample underwent a thermal treatment at 300 °C for 60 seconds each to dry the sample.

Ge doping: elemental germanium was introduced directly before the CZTS precursor deposition, known as an underlayer, via electron beam evaporation at a depstion rate of 0.8 Å s^{-1}.

Selenisation of CZTS: CZTS precursor films were enclosed in a rectangular graphite box with ~300 mg of selenium pellets and annealed in a tubular furnace, backfilled with Ar_2 and heated at 500 °C for 20 minutes. This selenisation and annealing, is essential in recrystallising the film to form micron sized CZTSSe grains. Further details on how the chalcogen exchange was controlled are described elsewhere[34, 35].

Solar cell device fabrication: The synthesised CZTSSe solar absorber films were assembled into solar cell devices in the following substrate configuration: Mo/(Ge)CZTSSe/CdS/intrinsic zinc oxide (i-ZnO)/indium tin oxide (ITO)/Ni:Al. The N-type CdS buffer (55 nm) was deposited via chemical bath using deionised water, cadmium sulphate, ammonium and thiourea after which the sample subject to 200 °C heat treatment in air for 20 minutes[21]. The resistive i-ZnO (35 nm) layer was deposited using pulsed DC sputtering sequentially before the transparent conducting oxide ITO layer (200 nm) was deposited using RF sputtering. Front contact finger bi-layers Ni (50 nn):Al (1 μm) were evaporated sequentially via electron beam evaporation through a mask before finally, a device area of 0.16 cm^2 was mechanically scribed.

b. Films characterisation

Film thicknesses was measured using a stylus profilometer (DektakXT). Surface and cross-section morphologies were studied by SEM (Tescan Mira 3) at 5 kV. Elemental analysis was performed using an attached EDS detector (Oxford Instruments X-max 150) with electron acceleration voltage of 7 kV for qualitative line scans and 20 kV for quantitative acquisitions. The crystallinity of films was studied with XRD (Rigaku SmartLab SE) using a CuK_α radiation source (λ = 0.15406 nm) operating at 2 kW equipped with Ni CuK_β filter- sample height alignment was performed before each acquisition. Raman spectroscopy was employed to further probe the structure using a Horiba microRaman spectrometer equipped with a 632.8 nm HeNe ion laser as excitation source calibrated with a Si control reference. Elemental depth profiling was performed using SIMS equipped with a Hidden Analytical gas ion gun and quadrupole detector operating an Ar^+ beam at 4 keV, raster area of ~500 μm x 500 μm and a grating of 10%.

c. Device measurements

Current-voltage measurements were performed using a source meter unit (Keithley 2400) connected to a 4-probe set-up. Solar cell devices were illuminated using a solar simulator (Abet Technologies sun 2000) at a simulated air mass (AM) 1.5 global spectrum calibrated using a c-Si reference solar cell. EQE measurements were performed using a spectral response monochromator system (Bentham Instruments M300) under illumination calibrated using a Si-InGaAs reference photodiode.

d. X-ray Photoelectron Spectroscopy and Energy-Filtered Photoemission of Electrons Microscopy

Photoemission measurements were carried out at the Bristol NanoESCA Facility (ScientaOmicron GmbH) system The system is made of conjoined chambers for XPS and EF-PEEM (base pressure: 2 × 10^{-11} mbar). Monochromatic Al kα (1486.7 eV) and non-monochromatic He I (21.2 eV) were used as excitation sources for XPS and EF-PEEM, respectively. Before the EF-PEEM and XPS, the samples were treated in preparation chamber maintained at UHV either by heating at 300°C for 1 hour or surface cleaned with 500 eV Ar^+ plasma etch for 5 mins. The surface composition of films before and after sample treatment was monitored with XPS. The EF-PEEM measurements were performed with nominal spatial resolution of 150 nm. An energy resolution of 140 meV was calibrated from Fermi-edge determination for a clean metallic surface, when operated at room temperature with an entrance slit of 0.5 mm and pass energy of 50 eV.

Author contribution statement

M.C.N. and G.Z. conceptualised of the project. M.C.N., D.T., D.J.F. and G.Z. established and discussed the methodology. M.C.N, B.F., X.X., M.J. and Y.Q. prepared the samples and contributed to solar cell fabrication. M.C.N, B.F., D.T., V. B., N.B., and G.Z. performed and analysed photovoltaic measurements. M.C.N., D.T., and S.C. performed and analysed the XRD and Raman measurements. M.C.N., A.S., and P.M. performed and analysed the SEM measurements. A.S., J.L., D.T., D.J.F. and N.A.F. performed, analysed and discussed the photoelectron spectroscopy measurements. M.C.N., D.T. and G.Z. wrote the first draft of the manuscript. G.Z., D.T. and D.J.F. supervised the project. G.Z., N.S.B., V.B., D.T., D.J.F. and N.A.F. provided funding for this study. All authors have reviewed and given approval to the final version of the manuscript.

Conflicts of Interest

The authors declare no conflict of interest.

Acknowledgements

This work was supported by the Engineering and Physical Sciences Research Council (EPSRC) via grants EP/S023836/1, EP/V008692/1, EP/V008676/1, EP/L017792/1, and EP/T005491/1. We are thankful for EPSRC strategic equipment grants EP/K035746/1 and EP/M000605/1. The authors also appreciate the support from the North East Centre for Energy Materials (NECEM) (EP/R021503/1), the British Council Newton Fund Institutional Links Grant (CRP01286) and the Royal Society of Chemistry (E20-9404). The authors thank and acknowledge use of the University of Bristol NanoESCA II Laboratory.

References

1. S. Siebentritt, *Thin solid films*, 2013, **535**, 1-4.
2. J. Zhou, X. Xu, B. Duan, H. Wu, J. Shi, Y. Luo, D. Li and Q. Meng, *Nano Energy*, 2021, **89**, 106405.
3. S. Y. Chen, A. Walsh, X. G. Gong and S. H. Wei, *Adv Mater*, 2013, **25**, 1522-1539.
4. S. Schorr, G. Gurieva, M. Guc, M. Dimitrievska, A. Perez-Rodriguez, V. Izquierdo-Roca, C. S. Schnohr, J. Kim, W. Jo and J. M. Merino, *J Phys-Energy*, 2020, **2**.
5. S. Kim, J. S. Park and A. Walsh, *Acs Energy Lett*, 2018, **3**, 496-500.
6. M. Kumar, A. Dubey, N. Adhikari, S. Venkatesan and Q. Qiao, *Energy & Environmental Science*, 2015, **8**, 3134-3159.
7. G. Rey, G. Larramona, S. Bourdais, C. Chone, B. Delatouche, A. Jacob, G. Dennler and S. Siebentritt, *Sol Energ Mat Sol C*, 2018, **179**, 142-151.
8. Y. F. Qi, Q. W. Tian, Y. N. Meng, D. X. Kou, Z. J. Zhou, W. H. Zhou and S. X. Wu, *Acs Appl Mater Inter*, 2017, **9**, 21243-21250.
9. R. J. Sun, D. M. Zhuang, M. Zhao, Q. M. Gong, M. Scarpulla, Y. W. Wei, G. A. Ren and Y. X. Wu, *Sol Energ Mat Sol C*, 2018, **174**, 494-498.
10. S. Kim, K. M. Kim, H. Tampo, H. Shibata and S. Niki, *Applied Physics Express*, 2016, **9**, 102301.

11. C. J. Hages, S. Levcenco, C. K. Miskin, J. H. Alsmeier, D. Abou-Ras, R. G. Wilks, M. Bär, T. Unold and R. Agrawal, *Progress in Photovoltaics: Research and Applications*, 2015, **23**, 376-384.
12. D. Tiwari, T. Koehler, X. Lin, R. Harniman, I. Griffiths, L. Wang, D. Cherns, R. Klenk and D. J. Fermin, *Chemistry of Materials*, 2016, **28**, 4991-4997.
13. D. Tiwari, M. Cattelan, R. L. Harniman, A. Sarua, N. Fox, T. Koehler, R. Klenk and D. J. Fermin, *Acs Energy Lett*, 2018, **3**, 2977-2982.
14. Y. E. Romanyuk, S. G. Haass, S. Giraldo, M. Placidi, D. Tiwari, D. J. Fermin, X. Hao, H. Xin, T. Schnabel and M. Kauk-Kuusik, *Journal of Physics: Energy*, 2019, **1**, 044004.
15. M. Neuschitzer, J. Marquez, S. Giraldo, M. Dimitrievska, M. Placidi, I. Forbes, V. Izquierdo-Roca, A. Pérez-Rodriguez and E. Saucedo, *The Journal of Physical Chemistry C*, 2016, **120**, 9661-9670.
16. S. Giraldo, M. Neuschitzer, T. Thersleff, S. López-Marino, Y. Sánchez, H. Xie, M. Colina, M. Placidi, P. Pistor and V. Izquierdo-Roca, *Adv Energy Mater*, 2015, **5**, 1501070.
17. S. Giraldo, E. Saucedo, M. Neuschitzer, F. Oliva, M. Placidi, X. Alcobé, V. Izquierdo-Roca, S. Kim, H. Tampo and H. Shibata, *Energy & Environmental Science*, 2018, **11**, 582-593.
18. M. Neuschitzer, M. E. Rodriguez, M. Guc, J. A. Marquez, S. Giraldo, I. Forbes, A. Perez-Rodriguez and E. Saucedo, *Journal of Materials Chemistry A*, 2018, **6**, 11759-11772.
19. S. Kim, K. M. Kim, H. Tampo, H. Shibata, K. Matsubara and S. Niki, *Sol Energ Mat Sol C*, 2016, **144**, 488-492.
20. Q. Guo, G. M. Ford, W.-C. Yang, C. J. Hages, H. W. Hillhouse and R. Agrawal, *Sol Energ Mat Sol C*, 2012, **105**, 132-136.
21. Y. Qu, G. Zoppi and N. S. Beattie, *Progress in Photovoltaics: Research and Applications*, 2016, **24**, 836-845.
22. S. Stølen, H. Johnsen, C. Bøe, O. Karlsen and T. Grande, *Journal of phase equilibria*, 1999, **20**, 17-28.
23. R. Sharma and Y. Chang, *Bulletin of alloy phase diagrams*, 1986, **7**, 68-72.
24. D. Tiwari, T. Koehler, R. Klenk and D. J. Fermin, *Sustainable Energy & Fuels*, 2017, **1**, 899-906.
25. X. Lin, T. Dittrich, S. Fengler, M. C. Lux-Steiner and A. Ennaoui, *Applied Physics Letters*, 2013, **102**, 143903.
26. D. Tiwari, M. Cattelan, R. L. Harniman, A. Sarua, A. Abbas, J. W. Bowers, N. A. Fox and D. J. Fermin, *Iscience*, 2018, **9**, 36-46.
27. M. Bär, T. Schnabel, J.-H. Alsmeier, S. Krause, N. Koch, R. G. Wilks and E. Ahlswede, *ACS Applied Energy Materials*, 2018, **1**, 475-482.
28. D. Tiwari, M. V. Yakushev, T. Koehler, M. Cattelan, N. Fox, R. W. Martin, R. Klenk and D. J. Femin, *ACS Applied Energy Materials*, 2022, **5**, 3933-3940.
29. A. Redinger, K. Hönes, X. Fontané, V. Izquierdo-Roca, E. Saucedo, N. Valle, A. Pérez-Rodríguez and S. Siebentritt, *Applied Physics Letters*, 2011, **98**, 101907.
30. X. Fontané, L. Calvo-Barrio, V. Izquierdo-Roca, E. Saucedo, A. Pérez-Rodriguez, J. Morante, D. Berg, P. Dale and S. Siebentritt, *Applied Physics Letters*, 2011, **98**, 181905.
31. G. Larramona, S. Levcenko, S. Bourdais, A. Jacob, C. Choné, B. Delatouche, C. Moisan, J. Just, T. Unold and G. Dennler, *Adv Energy Mater*, 2015, **5**, 1501404.
32. J. J. Scragg, T. Ericson, T. Kubart, M. Edoff and C. Platzer-Bjorkman, *Chemistry of Materials*, 2011, **23**, 4625-4633.
33. Y. Qu, G. Zoppi, R. W. Miles and N. S. Beattie, *Materials Research Express*, 2014, **1**, 045040.
34. Y. Qu, G. Zoppi and N. S. Beattie, *Sol Energ Mat Sol C*, 2016, **158**, 130-137.
35. Y. Qu, G. Zoppi, L. M. Peter, S. Jourdain and N. S. Beattie, *Japanese Journal of Applied Physics*, 2018, **57**, 08RC01.

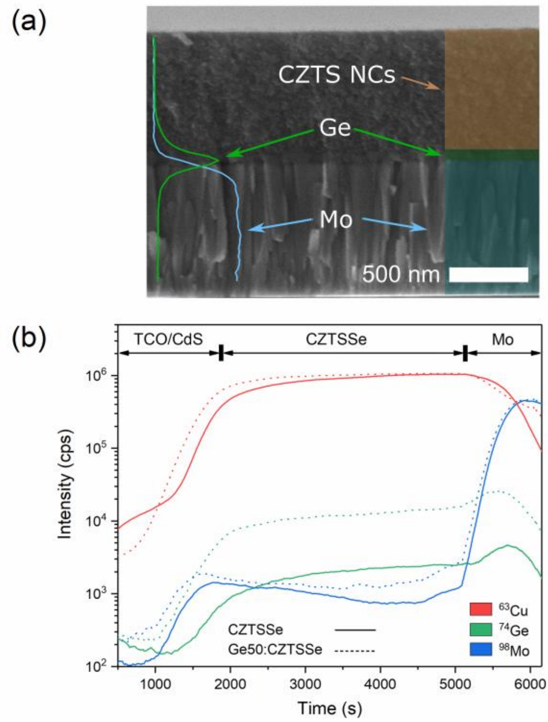

Figure 1. *(a) Elemental depth-profile of Ge and Mo acquired through EDS lines scan overlaid onto a of cross-sectional scanning electron micrograph of a CZTS precursor film. (b) SIMS depth profile of Ge, along with Cu and Mo indicating the construction of TCO/CZTS/Mo structure upon annealing for CZTSSe and Ge50:CZTSSe.*

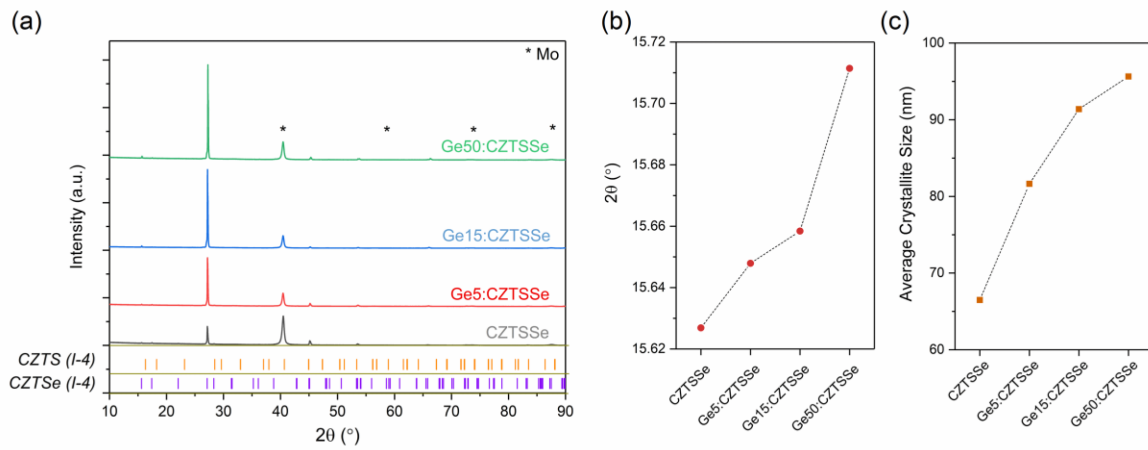

Figure 2. *(a) Structural analysis of CZTSSe films using XRD. XRD patterns of CZTSSe films with or without Ge along with Bragg reflections of kesterite (I-4)* Cu_2ZnSnS_4 *and* $Cu_2ZnSnSe_4$*. (b)* 2θ *shift of the (002) peak and (c) average crystallite sizes of (002) orientation CZTSSe films with respect to Ge amount.*

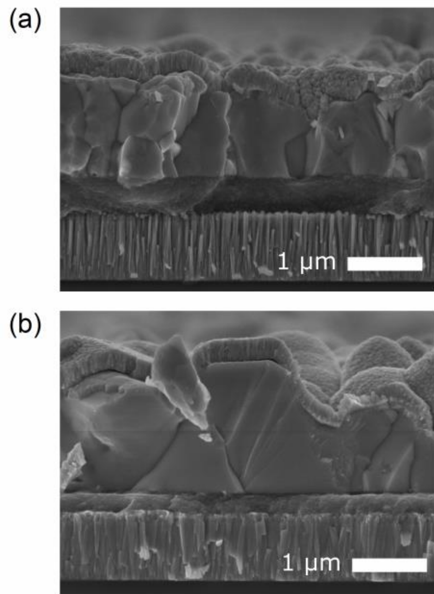

Figure 3. *Cross-sectional scanning electron micrograph of a complete solar cell device (SLG/Mo/(Ge)CZTSSe/CdS/i-ZnO/ITO) fabricating using (a) no Ge doping and (b) a 50 nm Ge underlayer.*

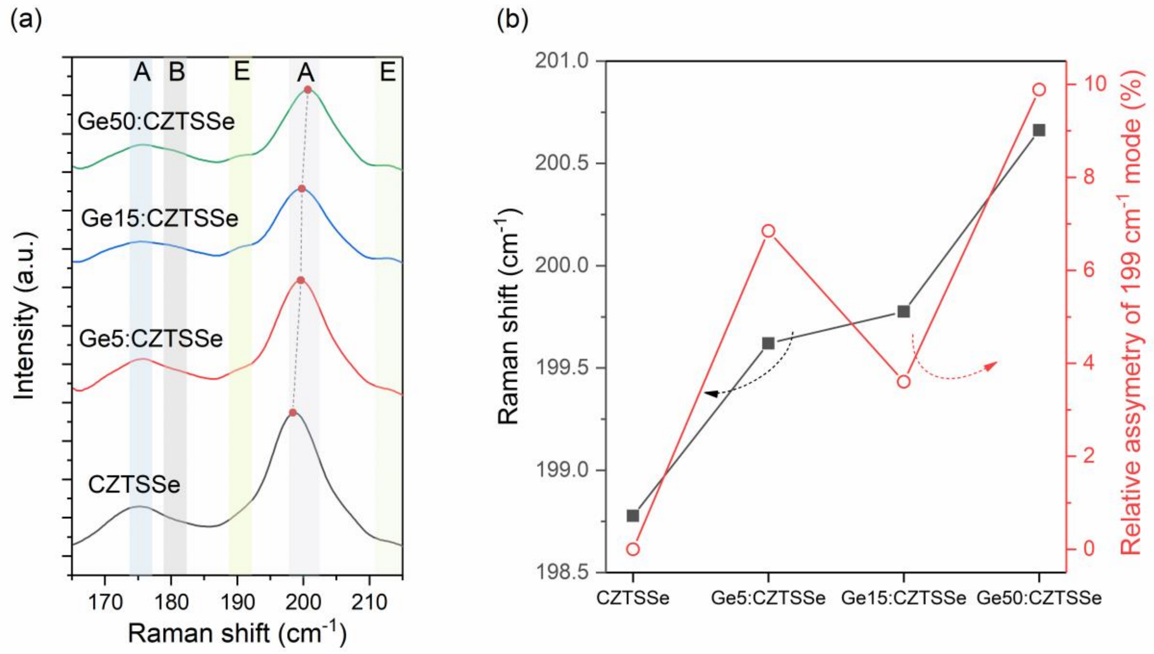

Figure 4. *(a). Raman spectra of CZTSSe films with or without Ge under 633 nm excitation. (b) Relative shift and asymmetry of the 199 cm^{-1} peak measured for the CZTSSe films with and without Ge.*

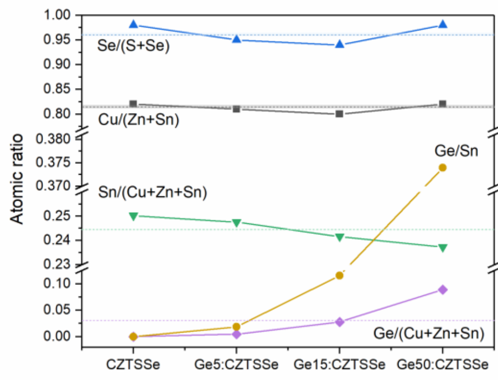

Figure 5. *Variation in bulk atomic ratios for CZTSSe films with and without Ge doping, calculated from quantitative EDS measurements.*

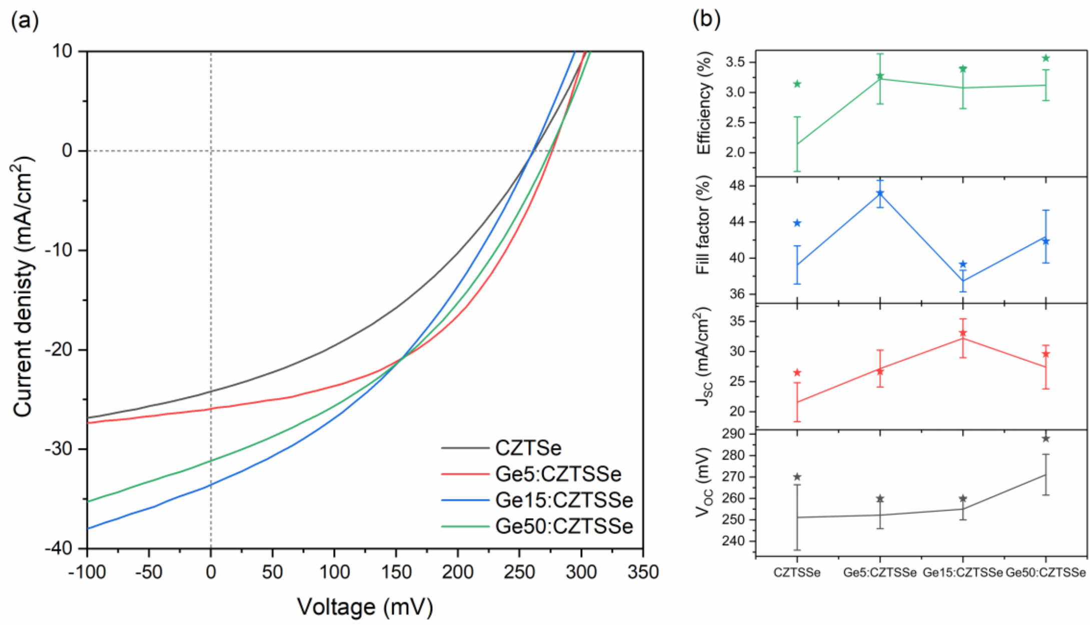

Figure 6. *CZTSSe device performance (a). J-V characteristics under simulated AM1.5G spectrum and (b) statistical analysis of performance parameters:* V_{oc}, J_{sc}, *fill factor and conversion efficiency, showing the standard deviation.*

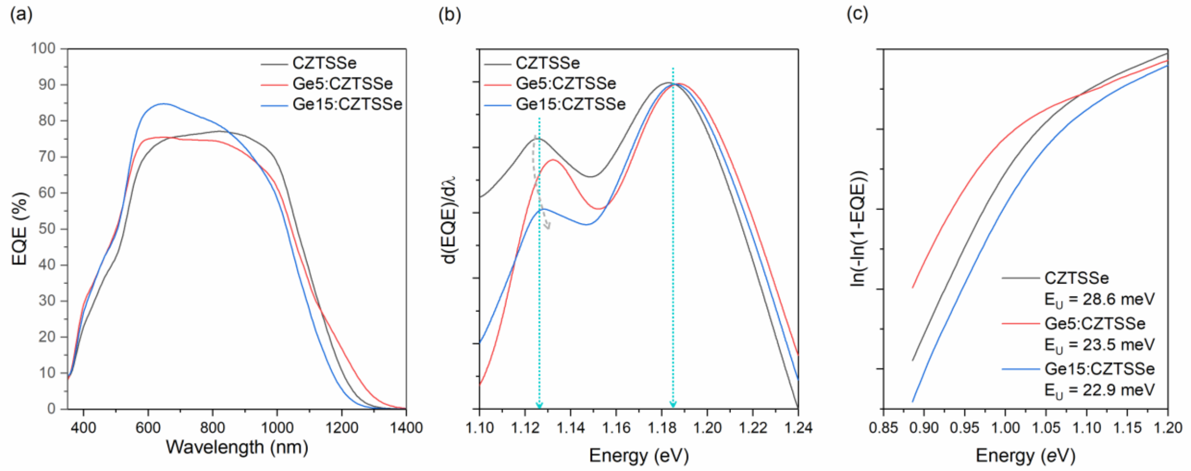

Figure 7. *(a) EQE for CZTSSe films with and without Ge. (b) Normalised first derivative of EQE with respect to wavelength at the CZTSSe absorption edge. (c) Urbach energy determination of CZTSSe from the sub-bandgap absorption region.*

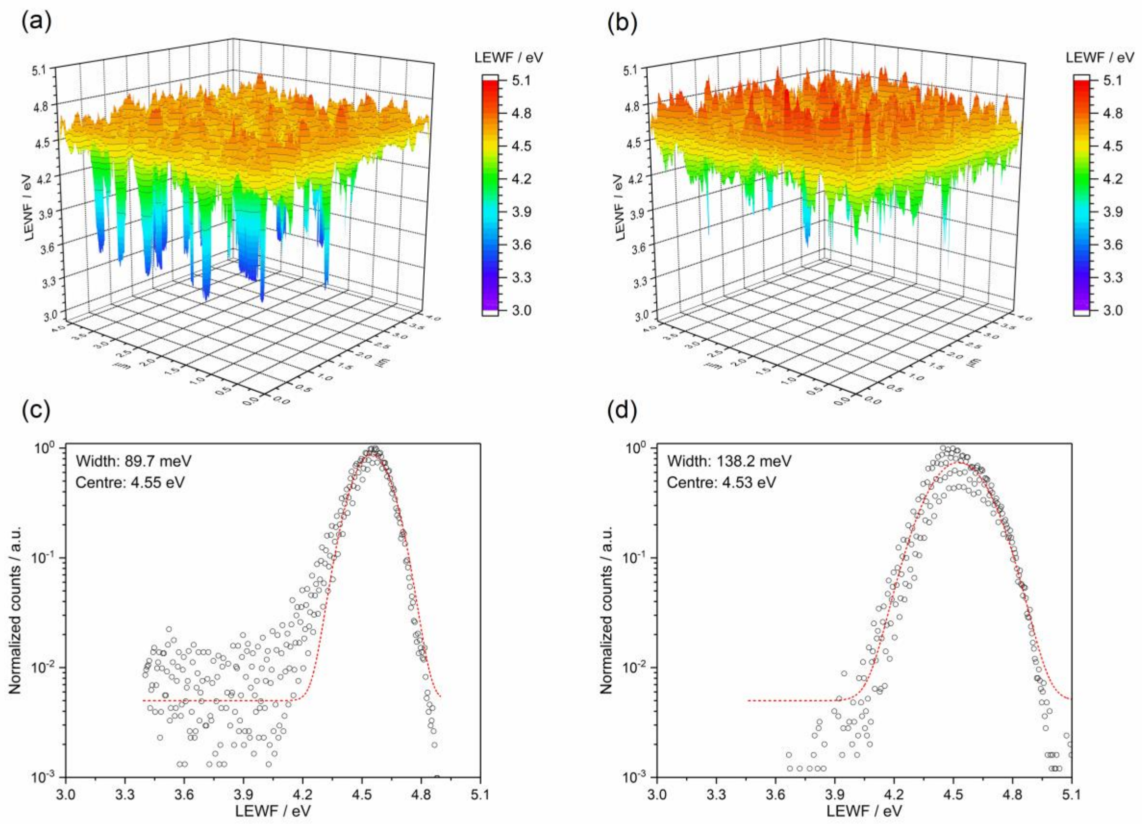

Figure 8. *LEWF maps showing the electronic terrain for (a) CZTSSe and (b) Ge5:CZTSSe after a 500 eV* Ar^+ *plasma etch treatment. Affiliated LEWF distribution showing spread of points (c) CZTSSe and (d) Ge5:CZTSSe.*

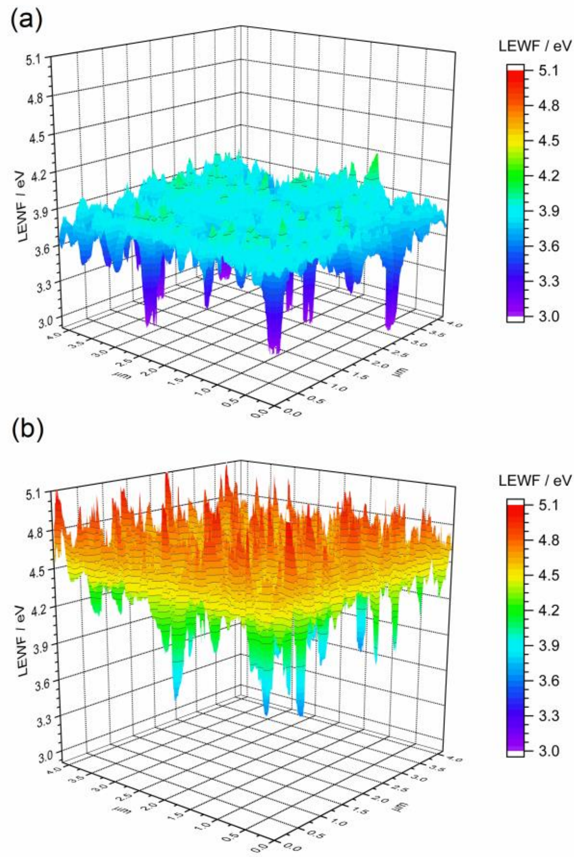

Figure 9. *LEWF maps which showing the electronic terrain for (a) CZTSSe and (b) Ge50:CZTSSe surfaces measured after heat a treatment at 300◦C in UHV for 1 hour.*